Supplemental Material

Supplemental movie S1. Movie of pVT initiation in LQT1 rabbits shown in Figure 1B.

Supplemental movie S2. Movie of pVT initiation in LQT1 rabbits in the presence of 4-AP shown in Figure 1C.

1. Experimental Methods

1.1 Optical Mapping

LQT1 rabbits of either sex, averaging 16.5 months old / 4.2 kg body weight / 9.14 g heart weight, were euthanized with buprenorphene (0.03 mg kg^{-1} IM), acepromazine (0.5mg kg^{-1} IM), xylazene (15 mg kg^{-1} IM), ketamine (60 mg kg^{-1} IM), pentothal (35 mg kg^{-1} IV), and heparin (200 U kg^{-1}). This investigation conformed to the current Guide for Care and Use of Laboratory Animals pub- lished by the National Institutes of Health and approved by the Lifespan Animal Welfare Committee in Rhode Island Hospital. Hearts were excised from the chest and retrogradely perfused through the aorta in a Langendorff perfusion system (Radnoti Glass Technology, Monrovia) with (in $mmol \cdot L^{-1}$) 130 NaCl, 24 $NaHCO_3$, 1.0 $MgCl_2$, 4.0 KCl, 1.2 NaH_2PO_4, 5 Dextrose, 1.25 $CaCl_2$, at pH 7.4, and gassed with 95% O_2 and 5% CO_2. Blebbistatin (5 μmol L^{-1}) was perfused to reduce movement artifact[1]. The AV node was ablated with a cautery device to slow heart rate in the range of 700 ms to 2 sec cycle length.

The optical apparatus has been previously described[2]. Fluorescence images from the anterior surface and LV free wall of the heart were captured using a CMOS camera (100 100 pixels, Ultima- L, SciMedia, Japan), and the field of view was set to 2.0×2.0 cm^2 (spatial resolution of 200×200 μm^2). The sampling rate was set to 1000 frames s^{-1}, and data was analyzed with a custom-built software program developed in Interactive Data Language (Exelis, Inc., Boulder). Hearts were stained with a voltage-sensitive dye, di-4-ANEPPS (Invitrogen, Carlsbad), using 25 μL of stock solution (1 mg ml^{-1} of dimethyl sulfoxide, DMSO) delivered through a bubble trap, above the aortic cannula. ECG and perfusion pressure were continuously monitored (PowerLab, ADInstruments, Colorado Springs).

The activation and repolarization time points at each site were determined from fluorescence signals by calculating $(dF/dt)_{max}$ and $(d^2F/dt^2)_{max}$. Data was filtered using a spatial Gaussian filter (3×3 pixel), and first/second derivatives were calculated using a temporal polynomial filter (3rd order, 13 points). Pixels with low signal-to-noise ratio determined by $(dF/dt)_{max}$ (lower than $3\times\sigma$ of baseline) and outliers of pixels determined by Grubbs' test were removed from analysis.

1.2 Patch clamp protocol

Isolation of cardiomyocytes by standard enzymatic techniques and patch-clamp recordings were performed as described previously[3] with some modifications as indicated. Ionic currents and action potentials were recorded at 34-36°C using standard whole-cell patch clamp technique with an Axopatch-200B amplifier, Digidata 1440A and pClamp 10 (Molecular Devices, Sunnyvale, CA). Pipette resistance was 2-4 MΩ. Capacitance and 60-70% of the series resistance were routinely compensated for. Action potentials were recorded under current clamp using 1.2 × threshold current injection. For recordings of AP and EADs in figures 2 and 5, the bath solution was Tyrode's solution containing (in mM): 140 NaCl, 5.4 KCl, 1.0 $CaCl_2$, 1.0 $MgCl_2$, 10 HEPES, and 5.6 glucose (pH 7.4). Pipette solution contained (in mM): 90 K-aspartate, 50 KCl, 5 MgATP, 5 NaCl, 1 $MgCl_2$, 0.1 Tris GTP, 10 HEPES, and 0.1 Rhod-2 K^+-salt (Invitrogen) (pH 7.2). All other patch clamp experiments were performed using the following pipette solution (in mm): 130 KCl, 5 $MgCl_2$, 0.36 $CaCl_2$, 5 EGTA, 5 Hepes, 5 glucose, 5 Mg-ATP, 5 Na_2-CrP, 0.25 Na-GTP (pH 7.2), whereas bath solution was varied to isolate different currents. IK1 and Ca^{2+} currents were recorded in normal Tyrode's solution. I_{K1} was measured with a voltage ramp from -120 mV to 60 mV. $I_{Ca,L}$ was measured using voltage steps between -40 mV to 40 mV from a holding potential of -50 mV. E-4031-sensitive rapid delayed rectifier current (I_{Kr}) isolated by current subtraction. I_{Kr} was recorded in a low K^+ and low divalent cation modified Tyrode's solution containing (in mM) 140 NaCl, 1.5 KCl, 0.33 NaH_2PO_4, 0.2 $MgCl_2$, 0.2 $CaCl_2$, 0.2 $CdCl_2$,5 HEPES, and 7.5 glucose (pH 7.4). I_{Kr} was recorded with voltage steps between -30 and 30 mV from a holding potential of -40 mV. I_{to} currents were recorded in a low-sodium modified Tyrode's solution containing: (in mM) 100 NMDG-Cl, 40 NaCl, 5.4 KCl, 0.33 NaH_2PO_4, 0.2 $MgCl_2$, 1 $CaCl_2$, 0.2 $CdCl_2$, 5 HEPES, and 7.5 glucose (pH = 7.4). To assist isolation of I_{to} current from other currents, 2.5 μM of E-4031, 30 μM of Chromanol 293B and 30 μM TTX were added to this bath solution. Voltage protocols for recording of I_{to} were voltage steps between -20 and 50 mV from a holding potential of -70 mV (Figure S1 panels A and B). For I_{to} inactivation measurements, P1 pulse varied from -60 mV to +50 mV for 500 ms followed by P2 at +50 mV for 500 ms (Figure S1 panels C and D). Data were sampled at 2.5–5 kHz and filtered at 1 kHz. Current–voltage relationships are normalized to the cell capacitances and presented as mean ± SEM.

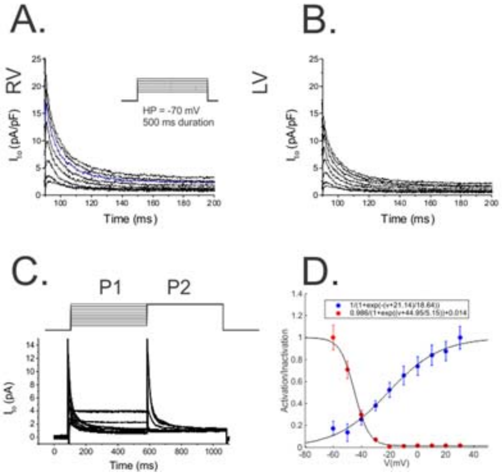

Figure S1. I_{to} traces from LQT1 in the presence of 50 nM isoproterenol. A) RV. The voltage clamp protocol is shown as an inset. B) LV. Note that Ito in RV has larger amplitude and slow inactivation kinetics than LV. C) P1P2 protocol for I_{to} inactivation (insert) and sample traces from LMC myocyte. D) Activation and Inactivation curve from LMC myocytes (n=12 LMC myocytes) using the inactivation protocol in panel C.

1.3 Patch clamp protocol for I_{to} recovery kinetics

Investigation of I_{to} recovery from inactivation was studied in TTX-free solution of avoid potential effect of TTX on I_{to}. To decrease effect of fast voltage-dependent inward sodium current on I_{to} measurement, we reduced driving force for sodium current by reducing extracellular sodium concentration from 140 mM to 40 mM by replacing sodium with N-Methyl-D-glucamine in the Tyrode solution. Calcium current was blocked by 0.2 mM $CdCl_2$, I_{Kr} was blocked by 2.5 μM E4031, and 50 nM isoproterenol was added to match the whole heart experiments. The patch pipette resistances were 2 to 4 MΩ when filled with 130 mM KCl, 0.36 mM $CaCl_2$, 5 mM EGTA, 5 mM HEPES, 5 mM glucose, 5 mM Mg-ATP, 5 mM Na_2-CrP, 0.25 mM Na-GTP, pH adjusted 7.2 with potassium hydroxide (KOH). The holding potential was -70 mV and two 500 ms depolarizing to +50 mV pulses were applied with varied time intervals between the pulses (0.05, 0.1, 0.2, 0.4, 0.6, 1, 2, 3, 5, 10, or 15 seconds). The time between subsequent pairs of depolarizing pulses was at least 30 seconds that allowed complete recovery of I_{to} after the second pulse of the previous protocol. I_{to} inactivation was fitted to a double exponential decay curve ($I_{to,fi}$ and $I_{to,si}$). The recovery kinetics of $I_{to,fi}$ and $I_{to,si}$ was further fitted to a double exponential curve to separate fast ($I_{to,f}$) and slow recovery components ($I_{to,s}$).

1.4 Confocal Ca^{2+} recording

Cytosolic and intra-SR Ca^{2+} changes were monitored using Leica TCS SP5 II confocal system in a line scan mode and Vm were simultaneously recorded with the patch-clamp technique[4]. Ca^{2+} transients were recorded in intact cells loaded with Fluo-3-AM at 0.25 Hz field stimulation in the presence of 50 nM isoproterenol. SR-Ca^{2+} uptake and leak were studied using Fluo-5N-AM in saponin-permeabilized myocytes at room temperature (Life Technologies, Grand Island, NY) and the following intracellular solution (in mM): 120 potassium aspartate, 20 KCl, 3 MgATP, 0.81 $MgCl_2$, 10 phosphocreatine, 5 U ml-1 creatine phosphokinase, 0.5 EGTA (pCa 7), 20 HEPES (pH 7.2), and 0.02 cAMP to activate PKA. Ryanodine receptor-mediated SR Ca^{2+} leak was visualized by blocking SERCA with 10 μM thapsigargin, a specific SERCA inhibitor. To measure SERCA-mediated Ca^{2+} uptake Fluo-5N loaded cells were treated with 5 mM caffeine to fully deplete SR Ca^{2+} and then RyRs were blocked with RuRed (40 μM) in Ca^{2+} free solution. Subsequently SR Ca^{2+} uptake was induced by reintroduction of 100 nM free [Ca^{2+}] in the presence of RyR blocker. Calcium transients and SR Ca^{2+} leak and uptake were analyzed using Leica Software, Origin 8.2 (OriginLab, Northampton,MA) and Image J (NIH, Bethesda, MA).

1.5 Western blotting

Western blot analyses were performed as previously described [5, 6] using RIPA buffer supplemented with phosphatase, calpain and protease inhibitors (Sigma, St. Louis MO). The levels of proteins involved in Ca^{2+} handling and their phosphorylation were assessed by immunoblot analysis using 40 μg of homogenates from left and right ventricular cell samples as described previously[3]. Primary antibodies used were: anti-RyR2, anti-Cav1.2α1c from ThermoScientic (Waltham, MA), anti-SERCA2a from SigmaAldrich (St.Luis, MO), anti-phospholamban (PLB) from Upstate (Lake Placid, NY), anti-phospho-PLB-T17 from Santa Cruz (Dallas, TX); anti-phospho-PLB-S16, anti- Na^+/Ca^{2+} exchanger (NCX1) from Millipore (Billerica, MA); anti-KChiP2, anti Kv1.4 and anti- Kv4.2 were from Alomone (Jerusalem, Israel). Custom made rabbit anti-phospho-RyR2-S2809 and anti-phospho-RyR2-S2815 were from Phosphosolutions (Aurora, CO). Expression levels of RyR2, SERCA, PLB, Cav1.2α1c, NCX1, KChiP2, Kv1.4 and Kv4.2 were assessed after normalization to the loading control, GAPDH. Phosphorylation levels of RyR and PLB at specific sites were normalized to the levels of RyR2 and PLB from the same samples run in parallel. Protein bands were visualized using the Super Signal West Pico kit (Pierce, IL) and quantified using ImageJ (National Institutes of Health) and Origin 8 (OriginLab, Northampton, MA) software.

2. Additional Experimental Results

2.1 Effect of 4-AP on APD in LMC hearts

LMC hearts (n=5) were paced at 2000 ms and APDs were measured in the absence and the presence of 0.5 mM 4-AP. The representative action potential traces from RV (red) and LV (black) are shown Figure S2A and the maps of APDs are shown in the bottom panel. 4-AP at 0.5 mM concentration prolonged APDs (36% increase from 196 ± 25 to 266 ± 52 ms at 0.5 Hz pacing rate, n=5 hearts) in LMC hearts. APD gradient did not change its direction between RV and LV in LMC hearts. Isoproterenol injection in the absence and the presence of 0.5 mM 4-AP did not trigger EADs despite APD prolongation in LMC hearts (n=0/5 hearts).

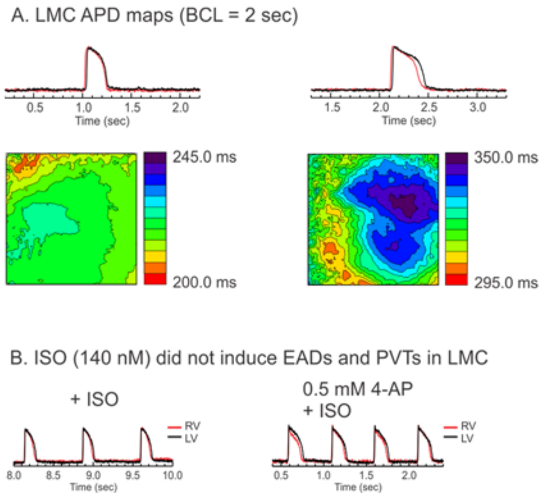

Figure S2. The effect of 0.5 mM 4-AP on action potentials in LMC hearts. A) Representative action potential traces (RV: red, LV: black) and APD maps in the absence and the presence of 4-AP in LMC heart. B) Isoproterenol injection in the presence of 0.5 mM 4-AP.

2.2 APD comparison between RV and LV myocytes isolated from LMC hearts

Action potentials were recorded from the RV and the LV myocytes isolated from LMC hearts under current clamp protocol. Figure S3A shows typical action potential recordings from RV (red) and LV (blue). EADs were rarely observed from LMC myocytes with 50 nM isoproterenol (panel B). APD data shows a trend to have shorter APD in RV (APD_{RV} = 214 ± 8 vs. APD_{LV} = 316 ± 25, p = 0.16, panel C).

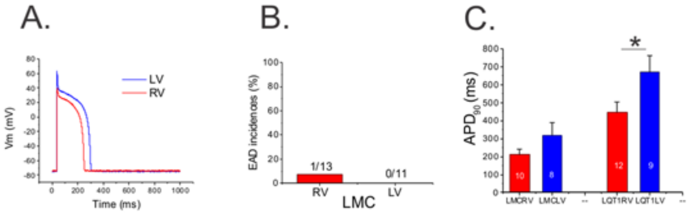

Figure S3. Action potential recordings of single myocytes isolated from LMC hearts. A) Representative Vm traces recorded from RV (red) and LV (blue) myocytes. B) EAD incidences from cells isolated from LMC hearts in the presence of 50 nM isoproterenol. C) APD_{90} of RV and LV cells isolated from LMC hearts. APDs from LQT1 were also plotted on the right side for comparison. Mean ± SEM

2.3 Additional voltage clamp results from LMC hearts

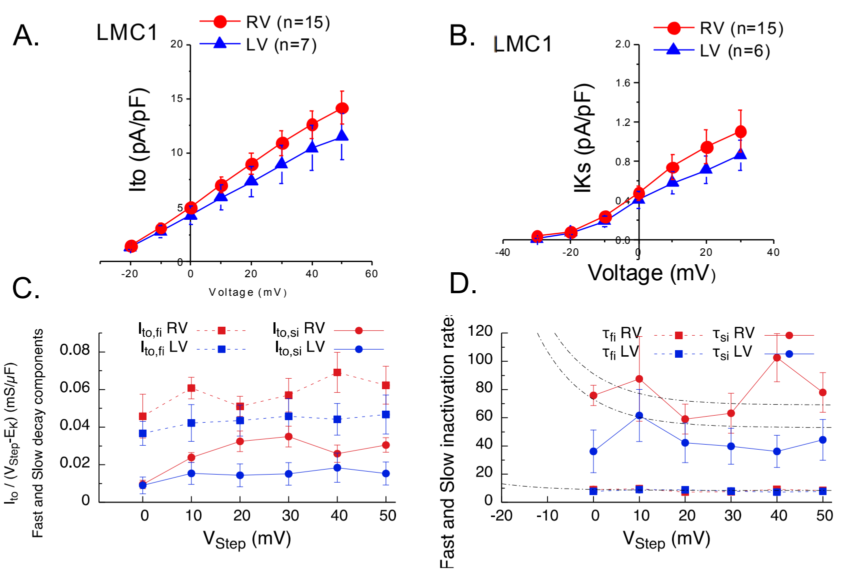

Figure S4. Measurements of K^+ currents in LMC cells. A) I_{to} peak current. B) I_{Ks} peak current. C) $I_{to,fi}$ and $I_{to,si}$ from RV and LV cells. D) τ_{si} and τ_{fi} from RV and LV cells. Neither I_{to} peak nor gating were found to differ between LMC and LQT1. I_{Ks} magnitude was used for computer modeling of LMC action potentials in Figure 7 panels A and F.

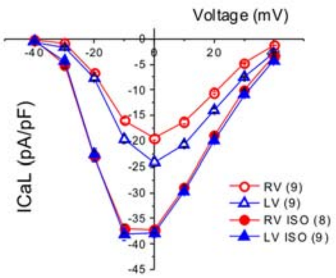

Figure S5. $I_{Ca,L}$ in the absence and the presence of 50 nM isoproterenol. In the absence of isoproterenol, $I_{Ca,L}$ shows slightly larger in LV cells but in the presence of isoproterenol $I_{Ca,L}$ did not show statistically significant differences between RV and LV cells.

2.4 Western blots of I_{to} and Ca^{2+} handling proteins

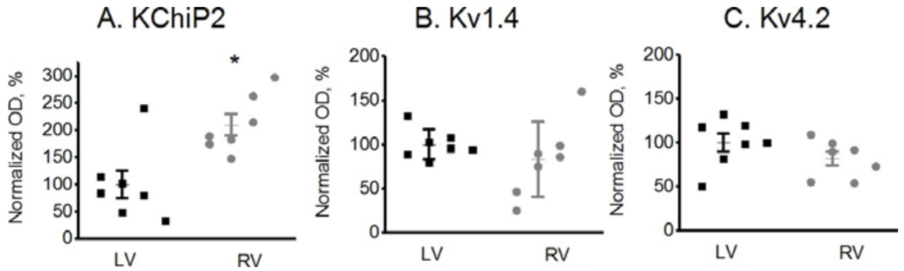

Figure S6. Optical density of KChiP2, Kv.14 and Kv4.2 in LV vs RV from 7 LQT1 hearts normalized to GAPDH expressed in % of mean for LV. Paired t-test, *$p < 0.05$.

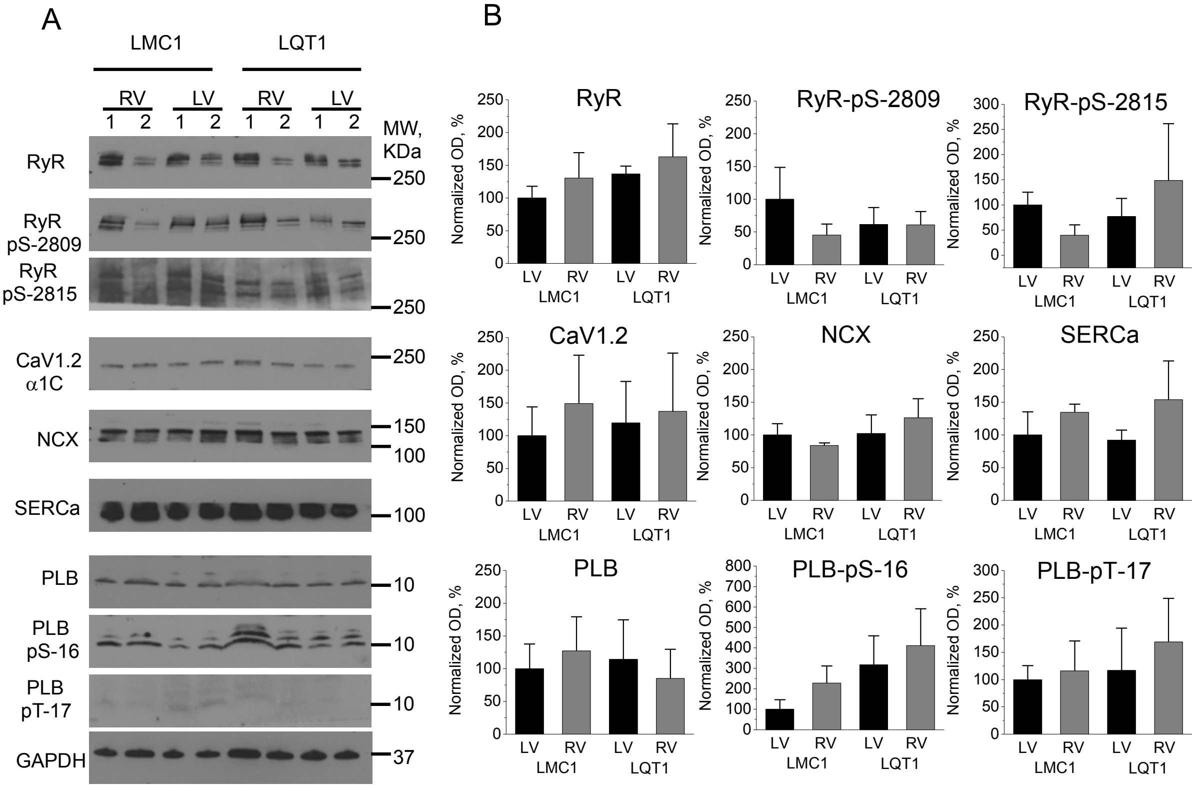

Figure S7. Unchanged expression levels and phosphorylation state of Ca^{2+} handling proteins in rabbit LQT1 myocytes from Left and Right ventricles. A) Representative western blots of RyR, RyR pS-2809, RyR pS 2815, CaV1.2, NCX, SERCA, PLB, PLB pS-16, PLB-pT17 in LV and RV myocytes from LQT1 and LMC. GAPDH was used as loading control. B) Pooled data for normalized optical density (OD, %) to loading control. Phospho RyR and phospho PLB were normalized to RyR and PLB respectively. One Way ANOVA showed no statistical significance at $p<0.05$, n=4.

2.5 Table of Summary

Table S1 EAD/pVT incidences and parameters of I_{to} from RV and LV of LQT1 hearts

	RV	LV	Statistics
pVT origin	8/9 hearts	1/9 heart	Fisher exact test, $p < 0.05$
pVT origin after 4-AP	1/5 hearts	4/5 hearts	Fisher exact test, $p < 0.05$
Cell Capacitance	119 ± 25 (n=43 cells)	168 ± 52 (n=38 cells)	t-test, $p < 0.01$
EAD incidences	8/12 myocytes	2/11 myocytes	Fisher exact test, $p < 0.05$
I_{to} amplitude (at 50 mV)	17.1±2.1 pA/pF (n=13)	12.4±1.4 pA/pF (n=12)	ANOVA, $p < 0.05$
$g_{to,fi}$ ($I_{to,fi}$ amplitude)	0.068 ± 0.0049 mS/μF	0.052 ± 0.0045 mS/μF	t-test, $p < 0.05$
τ_{fi} ($I_{to,fi}$ inactivation time constant at 50 mV)	8.8 ± 0.4 ms	7.8 ± 0.5 ms	Not significant
$g_{to,si}$ ($I_{to,si}$ amplitude)	0.033 ± 0.0052 mS/μF	0.018 ± 0.0021 mS/μF	t-test, $p < 0.05$
τ_{si} ($I_{to,si}$ inactivation time constant at 50 mV)	73 ± 6.7 ms	59 ± 6.9 ms	t-test, $p < 0.05$
$I_{to,f}$ amplitude	8.9 ± 1.7 pA/pF	5.3 ± 1.6 pA/pF	t-test, $p < 0.05$
τ_{fast} ($I_{to,f}$ recovery time constant)	19.5 ± 1.1 ms	19.5 ± 1.9 ms	Not significant
$I_{to,s}$ amplitude	22.4 ± 1.8 pA/pF	14.8 ± 0.44 pA/pF	t-test, $p < 0.05$
τ_{slow} ($I_{to,s}$ recovery time constant)	3.41 ± 0.33 s	3.13 ± 0.12 s	Not significant

3. Mathematical Modeling

We used a modified ventricular myocyte model of Ca^{2+} cycling coupled to membrane voltage (V_m) dynamics[6] to investigate the ionic mechanisms of EAD formation in LQT1 myocytes under conditions corresponding to the experiments. The model describes the bi-directional coupling of Ca^{2+} and V_m dynamics by incorporation of a full set of sarcolemmal currents including $I_{Ca,L}$, I_{NCX}, I_{Kr}, I_{to}, I_{K1}, and I_{NaK}, and also including (excluding) I_{Ks} for LMC (LQT1) myocytes.

To model the effect of β-adrenergic stimulation with isoproterenol (ISO), we increased the SERCA uptake rate by 50% and decreased the threshold by 40% (Table S1). We used the modified Hodgkin-Huxley model of LTCC, with releasing currents under voltage clamp fitted to experimental measurements under 50 nm ISO (Figure S11). The details of this model are described in section 2.3 of this supplement.

Computer simulations were carried out by pacing myocytes at 0.25 Hz until a steady state was reached. This protocol, and the external electrolyte concentrations (Table S1) were chosen to reproduce the conditions of isolated myocytes under patch clamp. This pacing protocol was applied to LMC and LQT1 myocytes from both LV and RV.

The gating kinetics of most of the ionic currents were largely unchanged, however, their conductance's were adjusted to better reproduce experimental measurements. Additionally, extra-cellular ionic concentrations were changed to match experimental conditions. A list of these parameters is given in Table S2.

The simulation code can be downloaded from the accompanying files in the supplementary material.

File Name	Description
README.pdf	Readme file for computer simulation code usage
LICENSE.license	Software license
cell.h	header file for computational routines
cell.cpp	program file with computational routines
OneSet.cpp	main function file

Table S2. Modified parameters

Parameter	Definition	Value
g_{Kr}	I_{Kr} conductance	$0.096\ mS/\mu F$ (MGWMN)
g_{Kr}	I_{Kr} conductance	$0.16\ mS/\mu F$ (HH)
g_{Ks}	I_{Ks} conductance	$0.17\ mS/\mu F$ (RV)
g_{Ks}	I_{Ks} conductance	$0.14\ mS/\mu F$ (LV)
g_{Ca}	Strength of $I_{Ca,L}$	$70\ mmol/(cm\ C)$
g_{NCX}	Strength of I_{NCX}	$0.756\ \mu M/s$
v_{up}	Strength of uptake	$0.6\mu M/s$
$[Ca^{2+}]_o$	External calcium concentration	$1\ mM$
$[Na^{+}]_i$	Internal sodium concentration	$5.1\ mM$
τ_s	Submembrane-myoplasm diffusion time constant	$1.5\ ms$
τ_p	RyR refractory period	$500\ ms$
α	Constant	80
g_{RyR}	Release current strength	$1.29\ sparks\ cm^2/mA$

3.1 Transient outward K$^+$ current (I$_{to}$)

Figures 3A and 3B demonstrate examples of measured I_{to} current and double exponential fit to these curves, characterized by the equation

$$I_{to} = I_{to,fi} e^{-t/\tau_{fi}} + I_{to,si} e^{-t/\tau_{si}} + I_{SS} \tag{1}$$

We model this current using a Hodgkin-Huxley type model of the form:

$$\begin{gathered} I_{to} = g_{fi} X_{to} Y_{to,fi} (V - E_K) + g_{si} X_{to} Y_{to,si} (V - E_K) \\ \frac{dX_{to}}{dt} = \frac{X_{to}^{\infty} - X_{to}}{\tau_{to,X}} \\ \frac{dY_{to,fi}}{dt} = \frac{Y_{to}^{\infty} - Y_{to,fi}}{\tau_{fi}} \\ \frac{dY_{to,si}}{dt} = \frac{Y_{to}^{\infty} - Y_{to,si}}{\tau_{si}} \\ \tau_{to,X} = \frac{9}{1 + e^{(V+3)/15}} + 0.5 \end{gathered} \tag{2}$$

where we use the symbol V in all equations to denote V_m for brevity of notation.

Since activation is much faster than inactivation, we calculate the steady state activation curve X_{to}^{∞} by dividing the total peak I_{to} current at each voltage by the K$^+$ driving force $F(V) = V - RT/F \ln([K^+]_o/[K^+]_i)$ where $[K^+]_o = 5.4\, mM$ under patch clamp conditions used to record this current. The conductance g_{fi} is determined using the relation $[I_{to,fi}/F(V)]_{50mV} = g_{fi}$ where $I_{to,fi}$ is determined from the double exponential fit given by Eq. (1), and similarly for g_{si}. The inactivation is calculated by dividing the steady state current I_{SS} by the total peak I_{to} current. These curves are shown in Figure 3F. Fitting to these curves yields the following

$$\begin{gathered} X_{to}^{\infty} = \frac{1}{1 + e^{-(V+10.06)/13.75}} \\ Y_{to}^{\infty} = \frac{1}{1 + e^{(V+41.97)/5.14}} \end{gathered} \tag{3}$$

In RV:

$$\begin{gathered} g_{fi} = 0.08\, mS/\mu F \\ g_{si} = 0.05\, mS/\mu F \\ \tau_{fi} = 8.4 + \frac{100}{1 + e^{(V+60)/10}} \end{gathered} \tag{4}$$

$$\tau_{si} = 80 + \frac{3000}{1 + e^{(V+60)/10}}$$

In LV:

$$g_{fi} = 0.08\, mS/\mu F$$
$$g_{si} = 0.025\, mS/\mu F$$
$$\tau_{fi} = 8.4 + \frac{100}{1 + e^{(V+60)/10}} \tag{5}$$
$$\tau_{si} = 50 + \frac{3000}{1 + e^{(V+60)/10}}$$

In both LV and RV, all timescales are in ms. g_{fi} and g_{si} are chosen to be slightly different from experimental fitting shown in Figure 3, because the later measurements showed that I_{to} in Figure 3 was not fully recoverd. Instead, the conductance's are from Figure 4B, where I_{to} was fully recovered with time interval between the first peak and the second >15 s. Figure 4B also shows that the fast components of I_{to} in RV and LV are the same, and the slow component in LV is half of that in RV. The forms of τ_{fi} and τ_{si} are taken from Mahajan et al.[14] The values of τ_{fi} and τ_{si} at high voltage are chosen to match the experimental measurements within standard error shown in Figure 3E. The values at the resting voltage are consistent with the measurements of I_{to} recovery kinetics using a double pulse protocol. The recovery kinetics was found to be well fitted by a double exponential with time constants approximately equal to 20 msec and 3 sec. Examination of the inactivation time course of I_{to} following the double pulse reveals that most of the fast recovering component inactivates quickly. However, a non-negligible fraction of the slowly recovering component inactivates rapidly (80% in LV, 40% in RV, Figure 4C). Consequently, the current mathematical formulation of I_{to}, decomposed as the sum of $I_{to,fi}$ and $I_{to,si}$, provides a reasonably good approximation to both the inactivation and recovery kinetics of measured I_{to}, even though neither $I_{to,fi}$ nor $I_{to,si}$ individually models $I_{to,f}$ or $I_{to,s}$ (traditionally associated with the fast and slowly recovering components of I_{to}).

3.2 Rapidly Activating Delayed Rectifier K$^+$ Current (I_{Kr})

Initial modeling was unsuccessful in producing I_{to} dependent EAD onset in LQT1 myocytes using the standard formulation of I_{Kr} by Zeng et. al.[7] Voltage clamp studies of the I_{Kr} current have suggested that Hodgkin-Huxley (HH) type models do not sufficiently reproduce observed behavior in I_{Kr} experiments[8-10]. A meta-analysis of multiple I_{Kr} models[11] shows that models that accurately portray the behavior of I_{Kr} have both deeper closed states of inactivation, and inactivation pathways which are not independent of the activation gate (a channel will typically need to activate before it can transition to the inactivated conformation). In accordance with these findings we chose to model I_{Kr} with 5 states based on the formulation of Mazhari et al.[12], depicted in Figure S8.

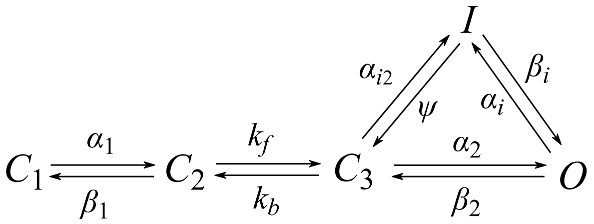

Figure S8. Schematic depiction of the Markovian transition between activation and inactivation states where *C*1, *C*2, and *C*3 correspond to closed states[12], *I* represents the inactivated state, and *O* the open state.

The rapidly activating delayed rectifier K+ current is given by:

$$I_{Kr} = g_{Kr}\sqrt{\frac{[K^+]_o}{5.4}}\,O(V - E_K) \tag{6}$$

with the rates of reactions

$$\begin{aligned}
\frac{dC_1}{dt} &= \beta_1 C_2 - \alpha_1 C_1\\
\frac{dC_2}{dt} &= k_b C_3 + \alpha_1 C_1 - \left(k_f + \beta_1\right)C_2\\
\frac{dC_3}{dt} &= \beta_2 O + \psi I + k_f C_2 - (\alpha_2 + \alpha_{i2} + k_b)C_3\\
\frac{dI}{dt} &= \beta_i O + \alpha_{i2} C_3 - (\alpha_i + \psi)I\\
\frac{dO}{dt} &= \alpha_i I + \alpha_2 C_3 - (\beta_i + \beta_2)O
\end{aligned} \tag{7}$$

where the transition rates are given by:

$$\begin{aligned}
\alpha_1 &= 0.007953e^{V/30.631250}\\
\beta_1 &= 0.083063e^{-V/69.176}\\
\alpha_2 &= 0.008511e^{V/21.167}\\
\beta_2 &= 0.003242e^{V/95.020218}\\
\alpha_i &= 0.044965e^{-V/25.197271}\\
\beta_i &= 0.187367e^{V/1467.569512}\\
\alpha_{i2} &= 0.000035e^{V/496052.439941}\\
\psi &= \frac{\alpha_{i2}\beta_2\alpha_i}{\alpha_2\beta_i}\\
k_f &= 0.300789
\end{aligned} \tag{8}$$

$$k_b = 0.135702$$

A total of 17 parameters including g_{kr} were fitted to I_{Kr} voltage clamp data averaged over 7 cells. E4031-sensitive current (I_{Kr}) was recorded with voltage steps between -30 and 30 mV from a holding potential of -40 mV as described in Methods 1.3. The initial parameters were chosen based on experimental data and previously published parameter sets in Mazhari et al.[12] and calculated τ values. The initial g_{Kr} was chosen based on the inactivation curve estimated from the tail current (see Figure S10 panel E). The optimization of 17 parameters were done using a simultaneous perturbation stochastic optimization algorithm[13] to accelerate initial fitting. Further optimization was performed using the genetic algorithm built in Matlab R2015b to search in parameter space for the best global minimum of the cost function defined as the least square error of the difference between experimental and modeling I_{Kr} time traces. We obtained an accurate fit of experimental measurements with this formulation, depicted in Figure S9.

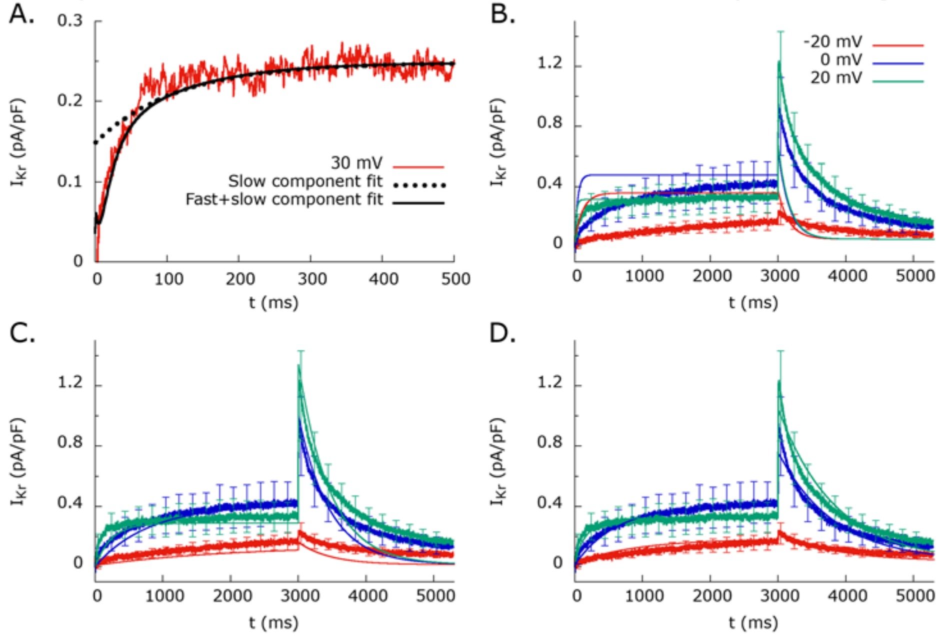

Figure S9. Comparison of different models of I_{Kr}. A) A representative trace of I_{Kr} activation at 30 mV. Double exponential fit to time course of I_{Kr} activation suggesting a single independent activation gate cannot reproduce the time-dependent gating of I_{Kr}. B) Model originally formulated by Luo and Rudy[16] using independent activation and inactivation gates. C) Similar Hodgkin-Huxley type 2-state model with parameters tuned to best fit experimental recordings. D) I_{Kr} modeled using the 5-state model described here. The error bars are standard deviation to show the scatter of data.

Comparing to the standard formulation of I_{Kr} by Zeng et al.[7], the 5-state model has two features that are important in data fitting and EAD onset. One feature is the accurate fit to experimental measurements (Figure S9D), due to the existence of deep closed states that produce double exponential I_{Kr} traces. With mono-exponential traces generated by HH type model, only the slow activation feature can be captured, shown in Figure S9 A. Importantly, as discussed below, this feature suffices to produce EADs (Figure S10A) even though it does not reproduce the two exponential time scales I_{Kr} activation kinetics (Figure S9 A). The other is the slow timescale of activation from -30 mV to 0 mV that is critical to promote EAD in RV. Without the slow activation timescale, as V_m traverses the EAD window, I_{Kr} current becomes so large that V_m spends a very short time in the window, allowing no sufficient time for I_{Ca} to recover.

To demonstrate that the significant aspect of this new model to the time course of repolarization and the onset of EADs is the slow timescale of activation, we reproduced the modeling results using an alternative HH-type formulation of I_{Kr}. This model approximately fits the experimental recordings of I_{Kr} under voltage clamp (Figure S9C). Equations of this model are as follows.

$$I_{Kr} = g_{Kr}\sqrt{\frac{[K^+]_o}{5.4}}X_{Kr}R(V)(V - E_K)$$

$$R(V) = \frac{1}{1 + e^{(V+53.5)/24.06}}$$

$$\frac{dX_{Kr}}{dt} = \frac{X_{Kr}^{\infty} - X_{Kr}}{\tau_{Kr}}$$

$$X_{Kr}^{\infty} = \frac{1}{1 + e^{-(V+7.78)/7.14}}$$

$$\tau_{Kr} = \left(\frac{1.466(V - 214.2)}{1 - e^{-(V-214.2)/17.18}} + \frac{0.01751(V + 58.93)}{e^{(V+58.93)/3.78} - 1}\right)^{-1}$$

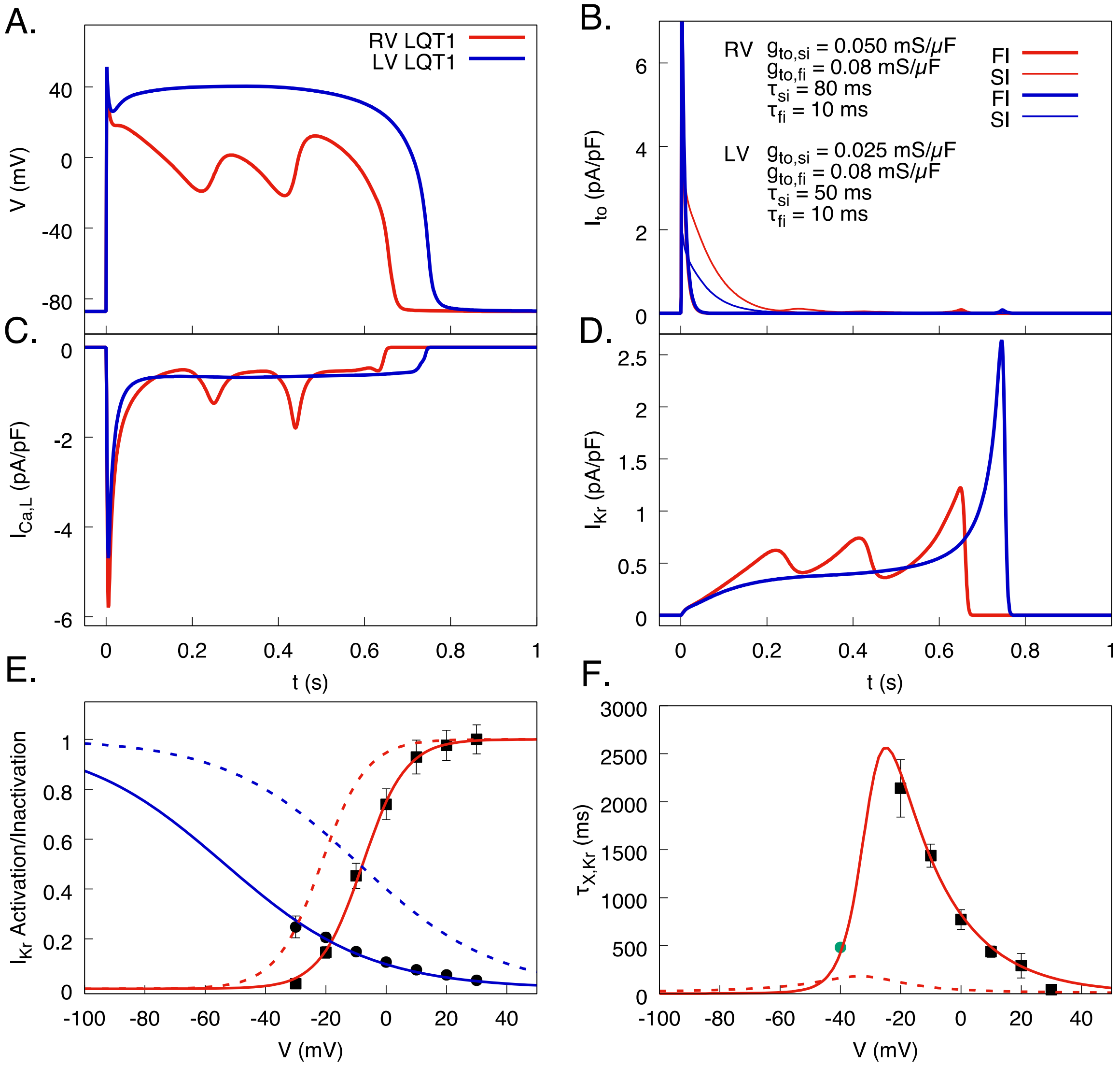

Figure S10. LQT1 myocytes in RV and LV using an alternative Hodgkin-Huxley formulation of I_{Kr}. A) Sample V_m traces for different I_{to} conductances including experimentally measured values from RV and LV cells. B) I_{to} traces broken into fast inactivating component (red thick in RV, blue thick in LV) and slowly inactivating component (red thin in RV, blue thin in LV) for action potentials in panel A. C) $I_{Ca,L}$ from RV (red) and LV (blue) during action potentials in panel A. D) I_{Kr} during action potentials in panel A. E) Activation and inactivation curves with Boltzmann fits used in HH model. Dashed lines denotes the equivalent curves used in Zeng et. al[7]. Experimental data is processed using procedures described in section 1.2. F) I_{Kr} activation time constant function fitting to activation data (black squares) and deactivation data (green circle). Dashed line denotes activation time used in Zeng et. al.[7] Data in E and F are from recordings in both RV and LV (n=7).

Figure S10 shows that this model reproduces a similar electrophysiological phenotype in both LV and RV as the 5-state model of I_{Kr} (Fig. 7 of the main text). The HH model also sheds light on the role of I_{Kr} in preferential EAD formation in the RV. In particular, computer modeling with both the multi-state and HH

I_{Kr} formulations with modified τ_{Kr} have shown that EADs occur preferentially in the RV under ISO stimulation. Our data shows that the activation kinetics of I_{Kr} are very slow for a range of V_m (-30 to 20 mV) but become faster above 20 mV, while the inactivation kinetics are instantaneous in the HH type model. In the RV, larger I_{to} causes V_m to traverse quickly in this range, delaying I_{Kr} activation. In particular, V_m spends a very short time of 10 ms from +40 mV to +20 mV, thereby preventing significant I_{Kr} activation (see Fig. 6E of the main text). V_m repolarizes further shortly within 200 ms in the +20 mV to -10 mV range and, over that range, the activation time of I_{Kr} increases approximately from 300 ms to 1.5 s (Figure S10F) allowing only partial activation of I_{Kr}. In contrast, the lower I_{to} in LV maintains V_m sustained at higher V_m, which causes I_{Kr} to move to inactivation quickly (see Panel E inactivation curve). As V_m traverses back to the range 0 mV to -25 mV, channels recover from inactivation quickly (from ~0% to ~20%, see panel E inactivation curve). In addition, due to slow time constant, the activation gate reaches to the steady state very slowly (from ~100% to ~70%), allowing large tail currents to repolarize AP quickly. The same principle can be seen in the multi-state I_{Kr} model where deactivation kinetics is slow compared to the quick transition from the inactivation to the open states, which allows channels to be accumulated in the open state, resulting in larger I_{Kr} during this voltage range to cause rapid repolarization without EAD formation in LV. These results support the theoretical interpretation that slow activation of I_{Kr} in the voltage range of -30 to 20 mV range is essential for EAD formation.

3.3 L-Type Ca^{2+} Current ($I_{Ca,L}$)

The original Mahajan et al.[14] model of $I_{Ca,L}$ has a very small window, and the parameters of this model are difficult to adjust to fit the voltage clamp data obtained under isoproterenol (ISO) stimulation. Therefore, we adopted the Hodgkin-Huxley model of $I_{Ca,L}$. Even though this model has a recovery kinetics from inactivation that is predominantly voltage-dependent, it can be used to incorporate the contribution of Ca^{2+} to rapid inactivation as well as to reproduce both the steady-state activation and inactivation curves, and therefore the size of the $I_{Ca,L}$ window.

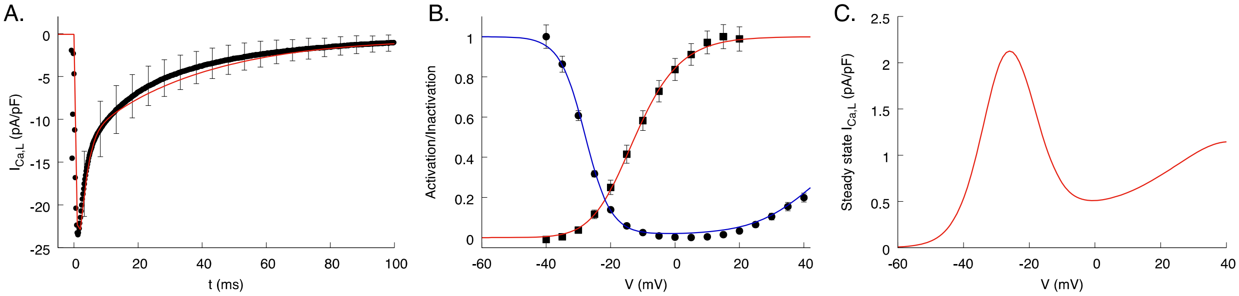

Figure S11. HH model of $I_{Ca,L}$ fit to experimental recordings of $I_{Ca,L}$ under 50 nM ISO. A) $I_{Ca,L}$ current recording for V_m step to 0 mV with 50 nM ISO. The error bars are standard deviation to show the scatter of data. B) Activation and inactivation curves. The blue curve is only for voltage-dependent inactivation. Ca^{2+}-dependent inactivation is shown in Eq. (10). C) Simulation generated steady-state $I_{Ca,L}$ window current in HH model.

The HH model of $I_{Ca,L}$ was fit to experimental recordings utilizing holding potential of –50 mV, followed by a P_1 pulse from –40 to +40 mV in 10mV steps lasting 250 ms, followed by a P_2 pulse to 0 mV. This procedure was performed with ISO. The peak of the P_1 pulse provided a measurement of steady-state activation (black squares in Figure S11B) and the peak of the P_2 pulse provided a measure of steady-state inactivation (black circles in Figure S11B). The time-course of the P_1 pulse constrained the kinetics of inactivation (Figure S11A). The window current of LTCC occurs during repolarization of the action potential, typically peaking between 0 and -30 mV. A critical feature of this model is that the window current remains high at V_m above 30 mV, which is the key in LV to maintain V_m at a high level, allowing I_{Kr} to be fully activated.

To improve the HH model of $I_{Ca,L}$, we used the same voltage clamp protocol as in the experiment to produce activation and inactivation simulation data, which were used to fit the experiment results shown in Figure S11B. The steady-state activation d^{∞} and inactivation f^{∞} curves were mainly changed during this procedure. Then Ca^{2+}-dependent inactivation f_{Ca}^{∞} was carefully chosen so that the simulation-generated traces fitted the experimental traces within standard devation shown in Figure S11A. The equations we found from fitting are as follows:

$$
\begin{aligned}
I_{Ca,L} &= g_{Ca,L} d f f_{Ca} i_{Ca} \\
\frac{dd}{dt} &= \frac{d^{\infty} - d}{\tau_d} \\
\frac{df}{dt} &= \frac{f^{\infty} - f}{\tau_f} \\
\frac{df_{Ca}}{dt} &= \frac{f_{Ca}^{\infty} - f_{Ca}}{\tau_{f_{Ca}}} \\
i_{ca} &= \frac{4P_{Ca}VF^2}{RT}\frac{c_s e^{2VF/RT} - 0.34[Ca^{2+}]_o}{e^{2VF/RT} - 1} \\
d^{\infty} &= \frac{1}{(1 + e^{-(V+17.6)/8.1})^2} \\
f^{\infty} &= \frac{0.98}{1 + e^{(V+27.66)/4.0432}} + \frac{0.5}{1 + e^{-(V-41)/8.93}} + 0.02 \\
f_{Ca}^{\infty} &= 0.7e^{-c_s/0.42} + 0.3e^{-c_s/9} \\
\tau_f &= \frac{75}{1 + e^{-(V-30)/4}} + 25 \\
\tau_{fCa} &= 3\ ms \\
\tau_d &= 0.8\ ms
\end{aligned}
\tag{10}
$$

For the simulations that HH model of I_{Kr} were used, the modified expressions are

$$
\begin{aligned}
f^{\infty} &= \frac{0.98}{1 + e^{(V+27.66)/4.0432}} + \frac{0.5}{1 + e^{-(V-46)/8.93}} + 0.02 \\
\tau_f &= \frac{43}{1 + e^{-(V-30)/6}} + 25
\end{aligned}
\tag{11}
$$

This is because HH model of I_{Kr} has a longer activation time scale at high voltage (Figure S9 & S10), therefore less depolarizing current is needed to reproduce the same behavior as MGWMN model of I_{Kr}.

3.4 Contribution of I_{to} inactivation to EAD onset

Our experimental and simulation data indicate that I_{to} is a major contributor to RV vs. LV AP characteristics and EAD genesis. Both I_{to} peak amplitude and its inactivation kinetics can contribute to phase 1 repolarization and determine EAD formation. Figure S12 shows EAD dynamics in the parameter space of inactivation time constant (τ_{si}) and conductance ($g_{to,si}$) of the slowly inactivating component of I_{to}. Panel A shows a heat map of EAD numbers and the parameter sets used for the representative computer simulationsfor RV and LV are marked with red and blue squares and experimental measurements are shown by red (RV) and blue (LV) filled circles together with standard errors. As shown in panels A, if I_{to} inactivation is slow (larger τ_{si}), less I_{to} conductance (smaller $g_{to,si}$) is needed to generate EADs. The RV and LV ranges of parameters fall well inside and outside the EAD window, respectively, consistent with observed AP phenotypes.

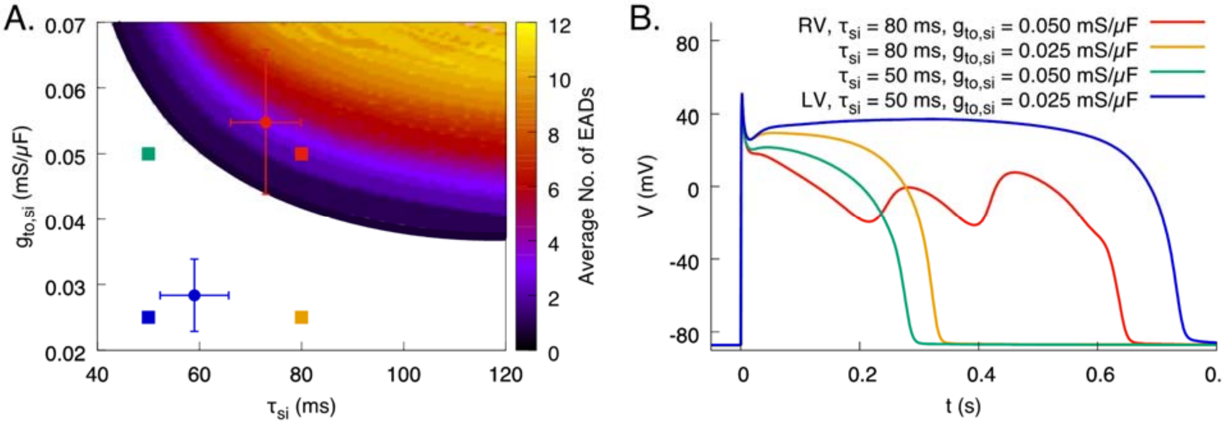

Figure S12. The contribution of $g_{to,si}$ and τ_{si} to EAD onset. A) Heat map with different $g_{to,si}$ and τ_{si} showing average number of EADs. The solid circles are experimental measurements from RV myocytes (red) and LV myocytes (blue), with τ_{si} from voltage clamp and $g_{to,si}$ from I_{to} recovery. The error bars are standard errors. B) Sample traces of V_m with different $g_{to,si}$ and τ_{si}, denoted by solid squares in A.

3.5 Ultra-long APDs in LV myocytes

The experimental recordings from LV myocytes show a large variability of APD in LV with several seconds of long APD (Figure 2A). Since there are cell-to-cell variations in ion channel expressions, we investigated whether variations in I_{Kr} and I_{CaL} can reproduce large variations in APD in LV cells. Figure S13 show that APD in LQT1 setting lacking I_{Ks} is highly sensitive to I_{Kr} and I_{CaL} conductances. Only 15% reduction in g_{Kr} or increase in $g_{Ca,L}$ produces ultra-long APDs in LV setting (Figure S13 red and green lines). When I_{to} alone is decreased by 15%, its effect on APD prolongation was moderate, suggesting that the balance between I_{Kr} and I_{CaL} is a major determinant of ultra-long APDs. It is important to note that ultra-long APDs still could not initiate EADs in all cases with LV setting, supporting that I_{to} is a dominant current to modulate EAD dynamics.

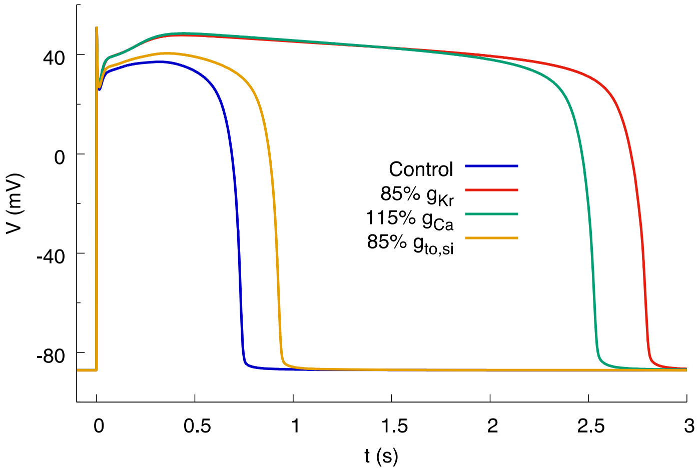

Figure S13. Variability of APD in LV obtained by changing g_{Kr}, $g_{Ca,L}$ and $g_{to,si}$. The blue line corresponds to the LV trace shown in Figure 7 in the main text, using the 5-state I_{Kr} model. The parameters were varied within 15% of the mean values based on the standard error of voltage clamp data.

3.6 Other modification of the model

3.6.1 Calcium cycling

Calcium cycling in the rabbit myocyte is based on the model by Shannon et al.[15], and improved by Mahajan et al.[14] In addition, the present model has two additional modifications. First, the function $g_{RyR}(V)$ was modified to obtain an experimentally realistic bell shape relationship between SR Ca^{2+} release amplitude and peak $I_{Ca,L}$ as a function of V_m (graded release). Second, we introduced a dyamical variable f_s that keeps track at the whole cell level of the fraction of Ca^{2+} release units (with colocation of L-type calcium channels (LCCs) and ryanodine receptor Ca^{2+} release channels (RyRs) in each unit) where a discrete release event (calcium "spark") has occurred. This latter addition enables us to model phenomenologically RyR refractoriness. Together, those two modifications allow us to reproduce calcium transients that are similar to those observed in the RV and LV (Figure 6). The modified Ca^{2+} cycling equations are:

$$\begin{aligned}\frac{dJ_{rel}}{dt} &= \frac{N_s'(t)Q\left(c_j'\right)c_j}{c^*} - \frac{J_{rel}}{T}\\ N_s'(t) &= -g_{RyR}(V)P_o i_{Ca} f_s\\ \frac{df_s}{dt} &= -\alpha N_s'(t) + \frac{(1-f_s)}{\tau_s}\\ g_{RyR}(V) &= \frac{g_{RyR}}{\left(1+e^{(V+25)/25}\right)\left(1+e^{-(V+37)/5}\right)}\end{aligned} \tag{12}$$

where c_j and c_j' are free Ca^{2+} concentrations in the junctional SR and the network SR. In this phenomenological model, $N_s'(t)$ is the spark rate in response to L-type Ca current, $Q\left(c_j'\right)$ describes the relationship of calcium release to SR calcium load, T is the relaxation time of junctional SR (JSR) release current to its steady-state value, and τ_s denotes the refractory period of RyRs after a spark. The units of c_j and c_j' are $\mu M v_{SR}/v_i$ $(\mu M/l\ cytosol)$, where v_{SR}/v_i is considered to be around 50, following Weber et al.[18] The parameter values are summarized in Table S2.

3.5.2 The slowly activating delayed rectifier K^+ current (I_{Ks})

We used the formulation based on Mahajan et al.[14], with τ_{xs2} equal to τ_{xs1}, and calcium dependent activation threshold shifted to $0.3\mu M$.

3.5.3 The fast sodium current (I_{Na})

The formulation for the fast sodium current is based on Mahajan et al., with the off rate of activation gate shifted by -16 mV:

$$\beta_m = 0.08e^{-(V+16)/11}$$

References

1. Fedorov VV, Lozinsky IT, Sosunov EA, Anyukhovsky EP, Rosen MR, Balke CW (17) and Efimov IR. Application of blebbistatin as an excitation-contraction uncoupler for electrophysiologic study of rat and rabbit hearts. *Heart Rhythm*. 2007;4:619-26.
2. Kim TY, Kunitomo Y, Pfeiffer Z, Patel D, Hwang J, Harrison K, Patel B, Jeng P, Ziv O, Lu Y, Peng X, Qu Z, Koren G and Choi BR. Complex excitation dynamics underlie polymorphic ventricular tachycardia in a transgenic rabbit model of long QT syndrome type 1. *Heart Rhythm*. 2015;12:220-8.
3. Brunner M, Peng X, Liu GX, Ren XQ, Ziv O, Choi BR, Mathur R, Hajjiri M, Odening KE, Steinberg E, Folco EJ, Pringa E, Centracchio J, Macharzina RR, Donahay T, Schofield L, Rana N, Kirk M, Mitchell GF, Poppas A, Zehender M and Koren G. Mechanisms of cardiac arrhythmias and sudden death in transgenic rabbits with long QT syndrome. *J Clin Invest*. 2008;118:2246-59.
4. Terentyev D, Rees CM, Li W, Cooper LL, Jindal HK, Peng X, Lu Y, Terentyeva R, Odening KE, Daley J, Bist K, Choi BR, Karma A and Koren G. Hyperphosphorylation of RyRs underlies triggered activity in transgenic rabbit model of LQT2 syndrome. *Circ Res*. 2014;115:919-28.
5. Belevych A, Kubalova Z, Terentyev D, Hamlin RL, Carnes CA and Gyorke S. Enhanced ryanodine receptor-mediated calcium leak determines reduced sarcoplasmic reticulum calcium content in chronic canine heart failure. *Biophys J*. 2007;93:4083-92.
6. Belevych AE, Sansom SE, Terentyeva R, Ho HT, Nishijima Y, Martin MM, Jindal HK, Rochira JA, Kunitomo Y, Abdellatif M, Carnes CA, Elton TS, Gyorke S and Terentyev D. MicroRNA-1 and -133 increase arrhythmogenesis in heart failure by dissociating phosphatase activity from RyR2 complex. *PLoS One*. 2011;6:e28324.
7. Zeng J, Laurita KR, Rosenbaum DS and Rudy Y. Two components of the delayed rectifier K+ current in ventricular myocytes of the guinea pig type. Theoretical formulation and their role in repolarization. *Circ Res*. 1995;77:140-52.
8. Wang S, Liu S, Morales MJ, Strauss HC and Rasmusson RL. A quantitative analysis of the activation and inactivation kinetics of HERG expressed in Xenopus oocytes. *J Physiol*. 1997;502 (Pt 1):45-60.
9. Clay JR, Ogbaghebriel A, Paquette T, Sasyniuk BI and Shrier A. A quantitative description of the E-4031-sensitive repolarization current in rabbit ventricular myocytes.

Biophys J. 1995;69:1830-7.

10. Liu S, Rasmusson RL, Campbell DL, Wang S and Strauss HC. Activation and inactivation kinetics of an E-4031-sensitive current from single ferret atrial myocytes. *Biophys J*. 1996;70:2704-15.
11. Bett GC, Zhou Q and Rasmusson RL. Models of HERG gating. *Biophys J*. 2011;101:631-42.
12. Mazhari R, Greenstein JL, Winslow RL, Marban E and Nuss HB. Molecular interactions between two long-QT syndrome gene products, HERG and KCNE2, rationalized by in vitro and in silico analysis. *Circ Res*. 2001;89:33-8.
13. Spall JC. Introduction to stochastic search and optimization: Estimation, Simulation, and Control: *Wiley*; 2003.
14. Mahajan, A., Shiferaw, Y., Sato, D., Baher, A., Olcese, R., Xie, L. H., ... & Garfinkel, A. (2008). A rabbit ventricular action potential model replicating cardiac dynamics at rapid heart rates. *Biophysical journal*, 94(2), 392-410.
15. Shannon, T. R., F. Wang, J. Puglisi, C. Weber, and D. M. Bers. 2004. A mathematical treatment of integrated Ca dynamics within the ventricular myocyte. *Biophys. J*. 87:3351–3371.
16. Luo, C. H., and Y. Rudy. 1991. A model of the ventricular cardiac action potential. Depolarization, repolarization and their interaction. *Circ. Res*. 68:1501–1526.
17. Shiferaw, Y., M. Watanabe, A. Garfinkel, J. Weiss, and A. Karma. 2003. Model of intracellular calcium cycling in ventricular myocytes. *Biophys. J*. 85:3666–3686.
18. Weber, C. R., V. Piacentino 3rd, K. S. Ginsburg, S. R. Houser, and D. M. Bers. 2002. Na-Ca exchange current and submembrane [Ca] dur- ing the cardiac action potential. *Circ. Res*. 90:182–189.